JGR Solid Earth

RESEARCH ARTICLE
10.1029/2021JB022335

Micromagnetic Calculations of the Effect of Magnetostatic Interactions on Isothermal Remanent Magnetization Curves: Implications for Magnetic Mineral Identification

Fan Bai[1], Liao Chang[1,2], Thomas A. Berndt[3], and Zhaowen Pei[1]

[1]Laboratory of Orogenic Belts and Crustal Evolution, School of Earth and Space Sciences, Peking University, Beijing, China, [2]Laboratory for Marine Geology, Qingdao National Laboratory for Marine Science and Technology, Qingdao, China, [3]Department of Geophysics, School of Earth and Space Sciences, Peking University, Beijing, China

Key Points:

- Micromagnetic calculations elucidate potential origin of multiple Gaussian remanent coercivity components
- The elongation distribution and grain morphologies strongly affect the shape of IRM curves for noninteracting fine-grained particles
- Magnetostatic interactions can overshadow the effect of grain morphologies and can also cause multiple Gaussian coercivity components

Supporting Information:

Supporting Information may be found in the online version of this article.

Correspondence to:

L. Chang,
liao.chang@pku.edu.cn

Citation:

Bai, F., Chang, L., Berndt, T. A., & Pei, Z. (2021). Micromagnetic calculations of the effect of magnetostatic interactions on isothermal remanent magnetization curves: Implications for magnetic mineral identification. *Journal of Geophysical Research: Solid Earth*, *126*, e2021JB022335. https://doi.org/10.1029/2021JB022335

Received 30 APR 2021
Accepted 7 JUL 2021

Abstract Isothermal remanent magnetization (IRM) curves are used widely in rock magnetic and environmental magnetic studies to characterize magnetic properties of natural samples. Previous theoretical and experimental investigations indicate that magnetostatic interactions can strongly affect the IRM behavior. In order to quantitatively investigate this effect, we modeled IRM curves and hysteresis properties for magnetite assemblages with variable morphologies (grain size, elongation, and shape) using the finite-element micromagnetic modeling code MERRILL. We also conducted an analytical study of IRM behavior for noninteracting single domain grains utilizing the Stoner–Wohlfarth model. It is found that multiple Gaussian components do not necessarily reflect multiple magnetic mineral populations. For example, magnetostatic interactions can produce coercivity distributions that resemble results of some samples containing a detrital and extracellular (D + EX) and a biogenic soft or hard (BS/BH) coercivity components. Simulated IRM curves for different morphologies of interacting flattened grains are similar, indicating that the effect of interactions can overshadow the effect of grain morphologies. Moreover, our micromagnetic and analytical calculations consistently indicate that the IRM curves for noninteracting fine-grained assemblages are mostly determined by grain shape (elongated or flattened) and elongation distributions of the magnetic mineral assemblages. Our simulations present possible outcome of IRM curves for magnetic mineral assemblages with controlled grain size, shape and microstructures, which provides important theoretical constraints on characterizing complex magnetic mineral components in natural samples through IRM curves and hysteresis.

Plain Language Summary Tiny magnetic mineral grains, often in the nanometer and micrometer size, in geological samples retain critical information about past environmental changes and geomagnetic field variations. Knowing the properties of magnetic minerals is crucial to decode magnetic mineral records. Decomposing isothermal remanent magnetization (IRM) curve into multiple magnetic mineral parts is a powerful technique, but is often complicated by the common presence of magnetic interactions where magnetic mineral grains are clumped to each other. This process is similar to attracting and repelling of magnets, but occurs at very small, microscopic scale. Here we have applied computer-modeling to calculate how neighboring magnetic grains affect the IRM curves. Our simulation results provide new physical constraints on analyzing IRM data, which is important to make robust environmental and geophysical interpretations.

1. Introduction

Rock magnetic and environmental magnetic investigations are mostly based on bulk magnetic measurements of natural samples that often contain magnetic mineral mixtures. Magnetic mineral unmixing, therefore, becomes increasingly important for determining the origin of constituent magnetic mineral components within natural samples for paleomagnetic and environmental magnetic interpretations (Heslop, 2015). Among magnetic mineral unmixing methods, decomposing isothermal remanent magnetization (IRM) curves has become a routine method to quantify multiple magnetic components (Egli, 2004b; Heslop, 2015; Roberts et al., 2019). Different IRM decomposing methods have been developed over the last few decades (Egli, 2003, 2004a, 2004b; Fabian & von Dobeneck, 1997; He et al., 2020; Heslop & Dillon, 2007;

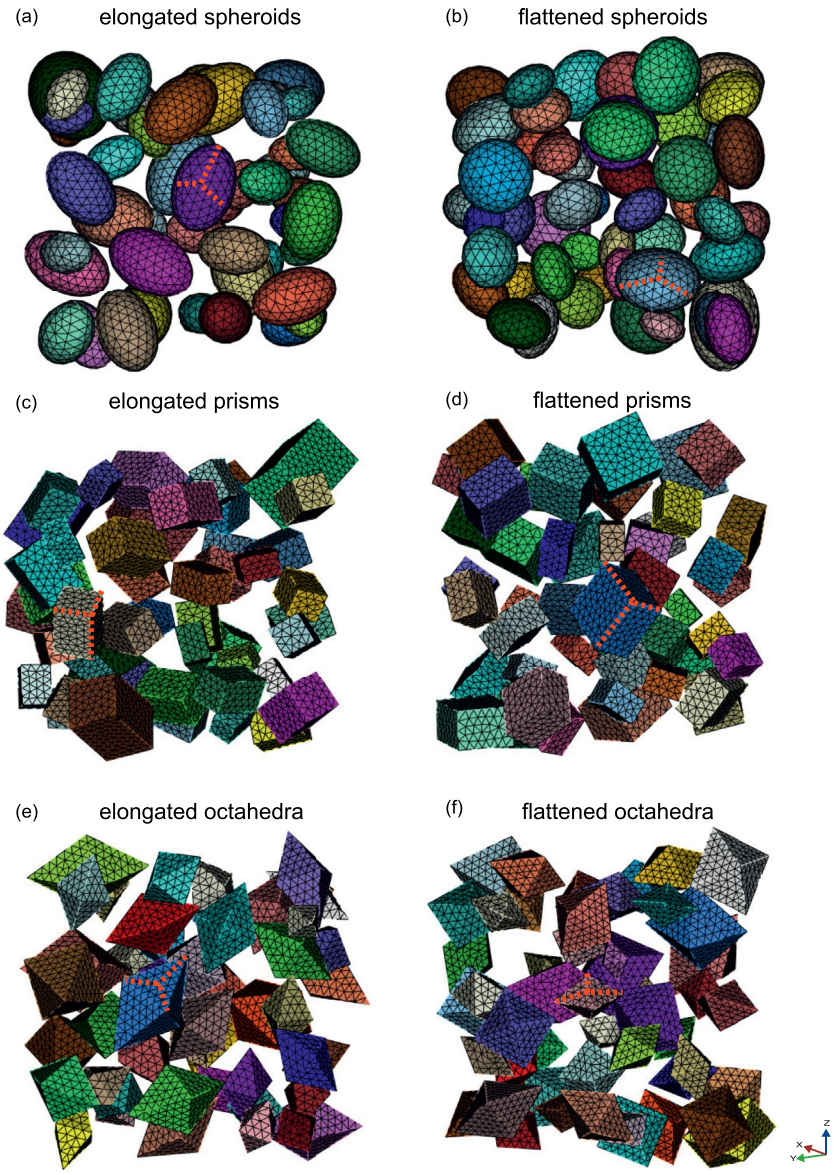

Figure 1. Examples of six types of model geometries for the interacting cases. Red dashed lines indicate three principal axes in each modeled grain geometry.

Heslop et al., 2002; Kruiver et al., 2001; Maxbauer et al., 2016, 2017; Stockhausen, 1998), most of which are based on the work of Robertson and France (1994) who suggested that experimental IRM curves could be fitted with cumulative log-Gaussian (CLG) functions. They demonstrated that IRM curves can often be described as the sum of several individual CLG curves–each is defined by a mean coercivity (B_c), a saturation IRM (SIRM), and a dispersion parameter (DP). There are, however, two main difficulties associated with this approach: (a) Highly overlapping coercivity distributions obtained from the CLG method complicate component analysis (Egli, 2004b). (b) In some cases, the experimental IRM curves cannot be fitted with ideal CLG functions in the presence of magnetostatic interactions, thermal activations, and others (Egli, 2004b; Heslop et al., 2004; Lees, 1997).

Regarding the latter, Kruiver et al. (2001) suggested that decomposing IRM curves into linear additive curves is only applicable if interactions are absent between IRM components. Several theoretical and numerical studies have investigated the effect of magnetostatic interactions on the IRM behavior: Many of these studies are either based on ideal single domain (SD) grains under dipolar approximations (e.g., Chang

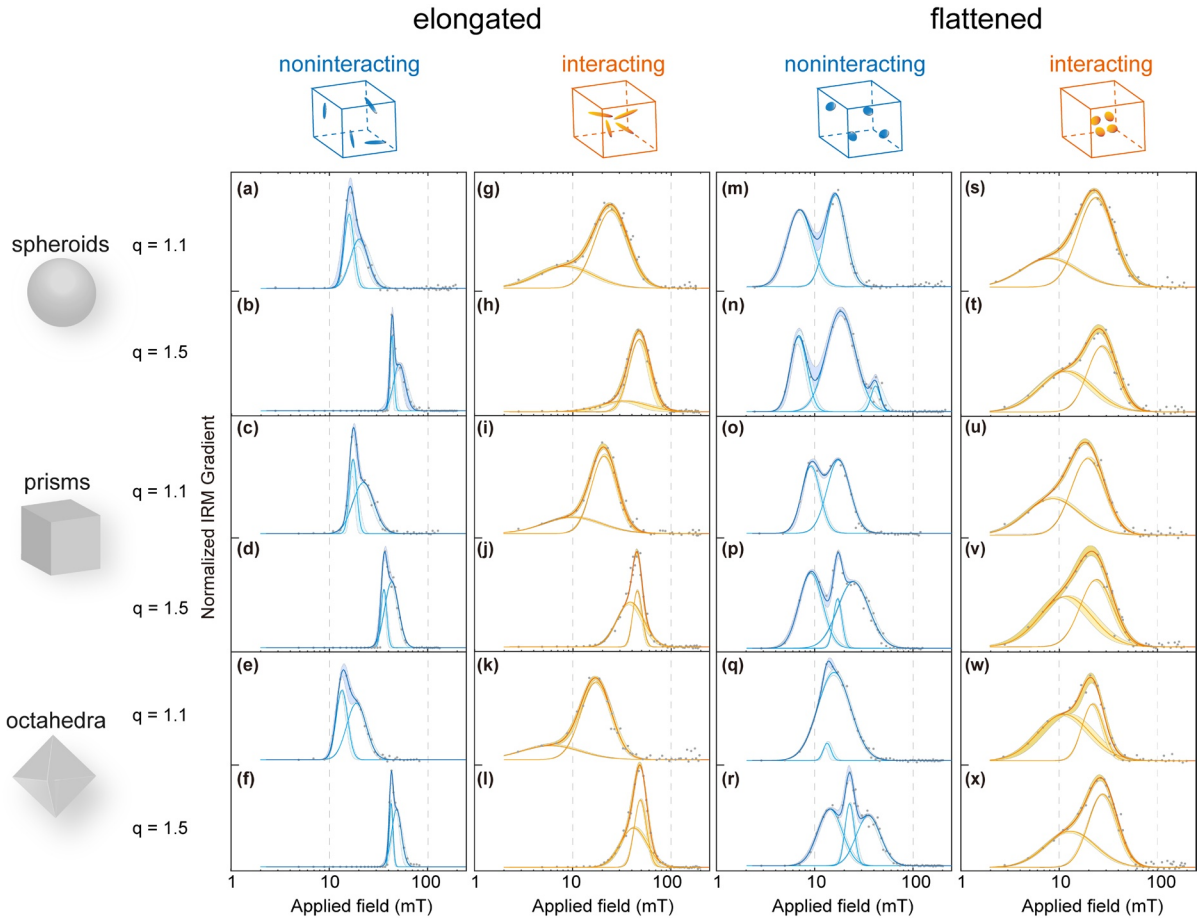

Figure 2. Examples of simulated IRM derivative curves and the corresponding Gaussian components for interacting and noninteracting elongated and flattened fine-grained spheroids, prisms, and octahedra (with q: 1.1 and 1.5). Gray dots: simulated raw data. Blue and orange indicate noninteracting and interacting particles, respectively: thick lines: total fit, thin lines: Gaussian components. Shaded area represents error envelopes of 95% confidence intervals.

et al., 2019; Fearon et al., 1990; Harrison & Lascu, 2014; Robertson & France, 1994; Sprowl, 1990), or solely related to variations of hysteresis parameters (e.g., Fearon et al., 1990; Ge & Liu, 2014; Harrison & Lascu, 2014; Muxworthy et al., 2003). Few systematic studies have been implemented to investigate the effect of magnetostatic interactions that control the shape of IRM curves.

In this study, we use three-dimensional (3D) finite-element (FE) micromagnetic simulations to investigate the effect of magnetostatic interactions on the IRM behavior for magnetite assemblages with variable grain morphologies. In addition, analytical calculations of IRM curves for noninteracting Stoner–Wohlfarth particles are presented and are compared to micromagnetic simulation results. 3D FE models are more representative for natural samples than dipolar-approximations, since they allow controlling of grain morphologies including grain size, elongation, and shape (e.g., spheroid, prism, and octahedron), magnetostatic interactions, and non-SD states (e.g., vortex states).

2. Methods

2.1. Micromagnetic Models

We have generated six types of magnetite grain geometries: spheroids, prisms, and octahedra, and each of them either elongated or flattened (Figure 1). For each geometry, a range of particle elongations q was modeled (q = 1.1, 1.2, 1.3, 1.4, 1.5, and a uniform distribution of particles in the q range from 1.0 to 1.5 denoted by "1–1.5"), where q is the ratio of the longest to the shortest axis in a particle (two out of the three axes of

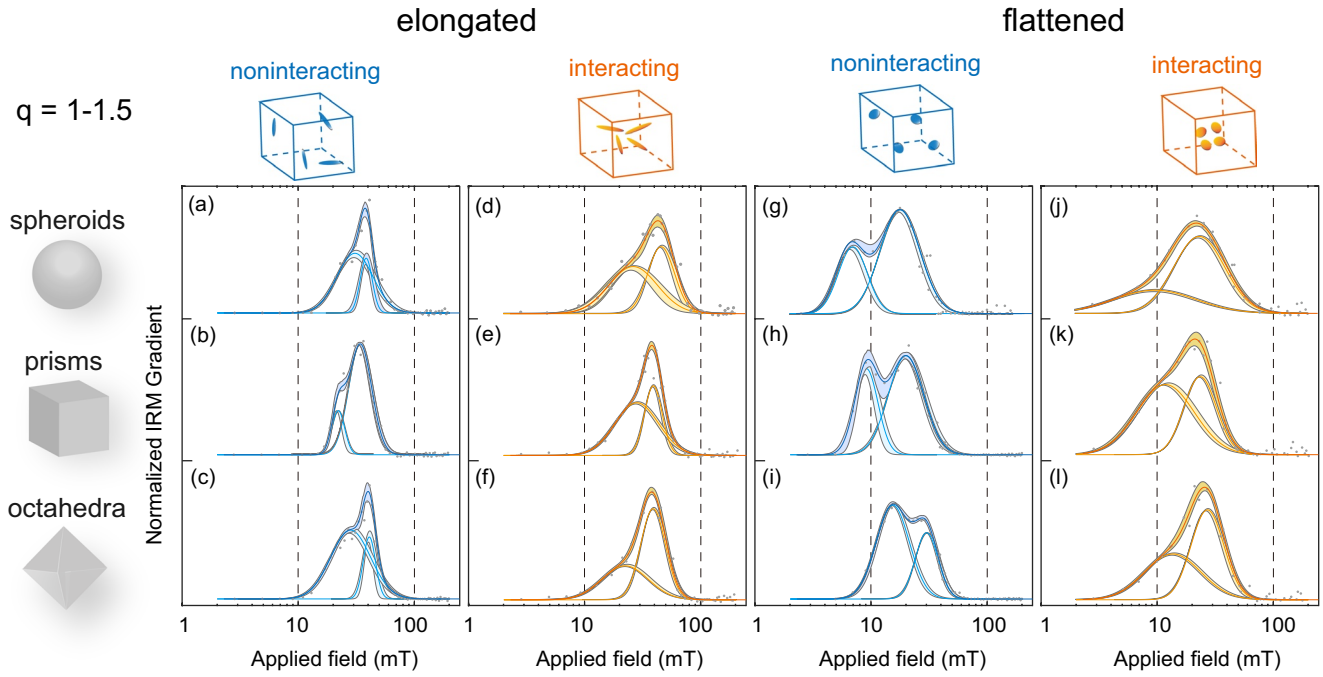

Figure 3. Simulated IRM derivative curves and the corresponding Gaussian components for ensembles with a range of elongations (q = 1–1.5). This figure has the same format as Figure 2.

the particle are always equal in length). Randomly oriented magnetite particles were selected from a log-normal grain size distribution (grain size is given as an equivalent diameter of a sphere d): (a) 50 particles from one fine-grained distribution for each type of geometry with each q (grain sizes from 25 to 84 nm, with mean grain size of 45.7 nm, and standard deviation of 9.7 nm) and (b) 35 particles from one coarse-grained distribution for elongated prisms with q = 1.5 (grain sizes from 50 to 180 nm, with mean grain size 101.7 nm, and standard deviation of 21.6 nm). These particles are randomly placed in a cubic space of volume V. Twenty to two hundred grain clusters were simulated for each set of parameters. We simulated two scenarios: interacting and noninteracting assemblages. The former had an average intra-particle distance (distance between grain border to grain border) of 22.5 and 50 nm, the latter of 450 and 1,000 nm (i.e., negligible interactions) for clusters of fine-grained and coarse-grained particles, respectively.

All models were generated and meshed with tetrahedral elements using the FE software Trelis (Trelis, 2021). We used mesh sizes of 8 and 9 nm for fine-grained and coarse-grained magnetite ensembles, respectively. Micromagnetic simulations were performed using the FE micromagnetic modeling software package MERRILL (Ó Conbhuí et al., 2018) version 1.3.3. Cubic magnetocrystalline anisotropy was taken into consideration, where magnetite's easy axis [1 1 1] is rotated to align with the direction of particle elongation. The conjugate gradient method was chosen to find energy minima. Domain states were visualized using ParaView (Ahrens et al., 2005; Ayachit, 2015).

2.2. Analytical Models for SD Stoner-Wohlfarth Grains

Our analytical calculations of remanent coercivities utilize the Stoner–Wohlfarth model (Stoner & Wohlfarth, 1948) developed by Dunlop & Özdemir (1997), where only external field energy and demagnetizing field energy are considered. The remanent coercivity B_k is calculated following Equations 1–5 (Dunlop & Özdemir, 1997):

$$B_k = \left(N_b - N_a\right)M_s \quad (1)$$

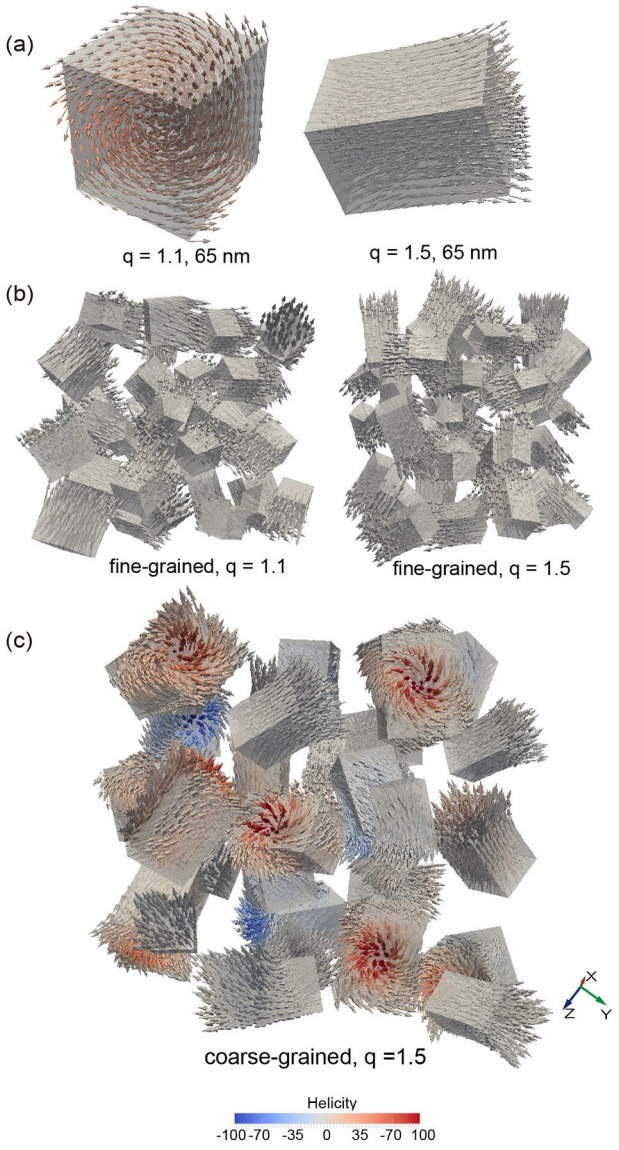

Figure 4. Remanent domain states at zero field for (a) noninteracting fine-grained prisms, (b) interacting fine-grained prisms, and (c) interacting elongated coarse-grained prisms with $q = 1.5$. Single prisms in (a) represent domain states of noninteracting particles (i.e., 65 nm long) because particles switch their moments independently in the absence of interactions. Colors indicate helicity.

$$B_0 \sin(\varphi - \theta) = \frac{1}{2}(N_b - N_a) M_s \sin(2\theta) \tag{2}$$

$$\tan^3 \theta = -\tan \varphi \tag{3}$$

where N_a and N_b are the demagnetizing factors, B_0 is the applied field, φ represents the angle between the grain long axis and B_0, B_0 rotate saturation magnetization M_s through an angle θ away from the long axis. Demagnetizing factors for elongated ellipsoidal particles are calculated following Osborn (1945):

$$N_a = \frac{1}{m^2 - 1}\left[\frac{m}{2\left(m^2 - 1\right)^{\frac{1}{2}}} \times \ln\left(\frac{m + \left(m^2 - 1\right)^{\frac{1}{2}}}{m - \left(m^2 - 1\right)^2}\right) - 1\right] \tag{4}$$

$$N_b = \frac{m}{2\left(m^2 - 1\right)}\left[m - \frac{1}{2\left(m^2 - 1\right)^{\frac{1}{2}}} \times \ln\left(\frac{m + \left(m^2 - 1\right)^{\frac{1}{2}}}{m - \left(m^2 - 1\right)^2}\right)\right] \tag{5}$$

where $m = a / c$, a, and c represent the long and short axis of the particle, respectively.

If $B_k \le B_0$, we consider that particles reversed their magnetic moments. The probability density function for φ of randomly oriented particles was given by: $p = \left(\sin \varphi\right)^2$. Ten thousand random orientations were generated for each set of q (i.e., $q = 1.1$, 1.2, 1.3, 1.4, 1.5, and 1–1.5 with a uniform distribution and a lognormal distribution with mean $q = 1.21$, and standard deviation of 0.071) to represent noninteracting grains.

2.3. Simulations of Hysteresis and IRM Properties

For micromagnetic simulations, back-field IRM curves, hysteresis loops, and first-order reversal curves (FORC; Roberts et al., 2000) were calculated. Hysteresis parameters, including saturation remanent magnetization M_{rs}, coercivity B_c, and remanent coercivity B_{cr} were extracted. Parameters were obtained by stacking 20–200 simulated curves. Back-field IRM curves with 56 field steps (2 mT for 0 to −50 mT, and 5 mT for −50 to −200 mT) were calculated. IRM derivative curves were fitted using Gaussian fitting package in MATLAB following the protocol of Kruiver et al. (2001). Each hysteresis loop was simulated from a 200-mT positive field to a 200-mT negative field along the [1 0 0] (x) axis with a 5-mT field step. Each FORC was obtained with a saturation field of 200 mT and a 5-mT field step so that 81 reversal curves were calculated. FORCs were processed using FORCinel 3.0 (Harrison & Feinberg, 2008) with a smoothing factor (SF; Roberts et al., 2000) of 4. For analytical models, IRM acquisition curves were calculated from 0 to 200 mT with a 2-mT step. We refer to the simulated IRM derivative curves as IRM curves in the following sections.

3. Results

3.1. Micromagnetic Simulation of IRM Curves

3.1.1. Fine-Grained Ensembles

In the absence of magnetostatic interactions, all the modeled IRM curves for elongated particles show a sharp increase on the left and a gradual decrease on the right (Figures 2a–2f and S1–S3). For modeled noninteracting flattened particles, two shoulders for small q (e.g., $q = 1.1$; Figures 2m and 2o) and three shoulders for large q are observed (e.g., $q = 1.3$, 1.4, and 1.5; Figures 2n, 2p, 2r, and S1–S3). Hence, IRM curves for noninteracting elongated and flattened particles require two Gaussian components (Figures 2a–2f) and at least two Gaussian components (Figures 2m–2r) to be adequately fitted, respectively.

In the presence of interactions, the left sharp increase of the IRM curves for the modeled elongated grains broadens (Figures 2g–2l and S1–S3) compared to noninteracting cases (Figures 2a–2f and S1–S3). IRM curves are all fitted with two Gaussian components: a narrower coercivity distribution superimposed on a broader coercivity distribution (Figures 2h, 2j, 2l, and S1–S3), except for the case of $q = 1.1$ where two relatively broad coercivity distributions are fitted (Figures 2g, 2i, and 2k). For interacting flattened particles, all the IRM curves have a similar asymmetric appearance without shoulders (Figures 2s–2x) compared to their noninteracting ensembles (Figures 2m–2r). All the IRM curves for interacting flattened particles can be fitted with two broad coercivity distributions.

3.1.2. Fine-Grained Ensembles With $q = 1$–1.5

Compared to simulations with a single q (Figure 2), simulations of ensembles with a range of q indicate, for noninteracting particles: (a) the sharp increase on the left of IRM curves are broadened for elongated particles (Figures 3a–3c) and (b) two shoulders are observed for flattened particles (Figures 3g–3i); for interacting particles: (a) IRM curves are fitted with two Gaussian components (Figures 3d–3f) similar to those for elongated particles (Figures 2g-2l) and (b) IRM curves retain the asymmetric appearance for flattened particles (Figures 3j–3l).

3.1.3. Coarse-Grained Ensembles

While simulated fine-grained particles are mostly SD (Figure 4b) with a minor proportion of vortex grains (i.e., for nearly equidimensional particles; Figure 4a), significant amount of vortex states exists with SD states in coarse-grained particles (Figure 4c). IRM curves for coarse-grained particles shift to lower coercivities compared to those for fine-grained particles (Figure 5). One narrow and two broad Gaussian components at lower fields appear for noninteracting coarse-grained ensembles (Figure 5a). In the presence of interactions, the IRM curve can be fitted with a narrow and a broad Gaussian component, similar to results for fine-grained ensembles (Figure 5b).

3.2. Analytical Simulation of IRM Curves for SD Stoner-Wohlfarth Grains

Simulated IRM curves for SD Stoner-Wohlfarth grains show similar features and B_{cr} values close to those obtained by micromagnetic simulations for noninteracting elongated assemblages (e.g., for elongated spheroids; Figures 2a, 2b, and 6a). For q with a normal distribution, analytical and micromagnetic calculations of IRM curves indicate similar B_{cr} values (Figure 6b). For q with a lognormal distribution, simulated IRM curve is different compared to that with a uniform q distribution (Figure 6b).

3.3. IRM and Hysteresis Parameters

Data points of DP against B_{cr} for noninteracting Gaussian components are scattered (Figure 7; Table S1). In contrast, for the two interacting Gaussian components, DP is generally inversely related to B_{cr} (Figure 7; Table S2). The relationship between DP and B_{cr} can be fitted with a linear function: $\Delta DP = -0.005\Delta B_{cr} + 0.31$.

Strikingly, clusters of flattened grains (both noninteracting and interacting) have hysteresis parameters (M_{rs}, B_c, and B_{cr}) nearly independent of grain elongation (Figures 8a–8c, S4, and S5; Table 1) – with the exception

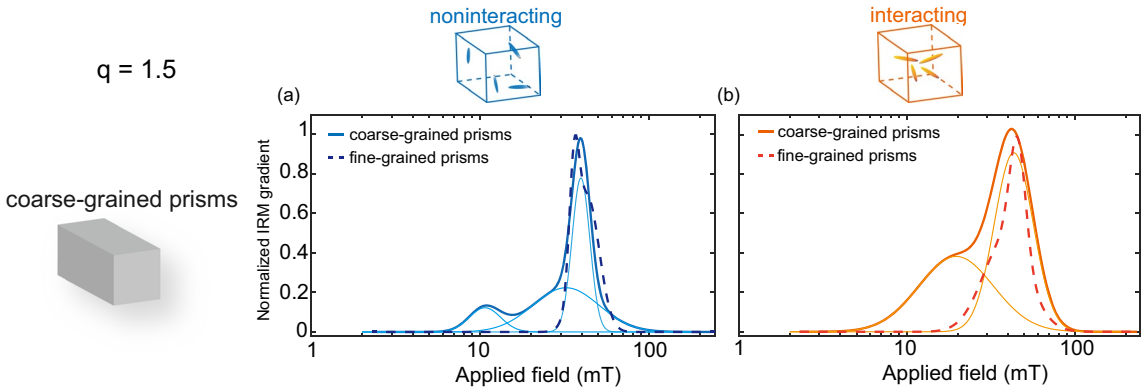

Figure 5. Smoothed IRM derivative curves and the corresponding Gaussian components for interacting and noninteracting elongated coarse-grained prismatic ensembles with $q = 1.5$. This figure has a similar format to Figures 2 and 3. Dashed lines: total fit for fine-grained elongated grain ensembles with $q = 1.5$.

of a slight increase of M_{rs} with respect to q for interacting grains (Figure 8a). For elongated grains, however, B_c and B_{cr} show a large increase with q. M_{rs}, B_c, and B_{cr} values are generally lower for interacting than for noninteracting ensembles–with the only exception of interactions generally increasing B_{cr} for flattened particles (Figure 8c).

We plotted the simulated hysteresis parameters in Day diagrams (Day et al., 1977, Figures 8d–8f) to show data trends, rather than domain state interpretation. In the absence of interactions, all data points for flattened particles appear in the top-left of the SD region (high M_{rs} and low B_{cr}/B_c) of the Day plot, similar to micromagnetic modeling results of individual flattened particles (Nikolaisen et al., 2020). In contrast, data for elongated particles scatter around the $M_{rs}/M_s = 0.5$ line. In the presence of interactions, all data points move toward the lower right region. Data plot well within the PSD region for interacting elongated spheroids (Figure 8d).

3.4. FORC Diagrams

Simulated FORC diagrams for noninteracting particles with a large q contain a central ridge peak and a negative distribution in the lower-left region (e.g., $q = 1.5$ for elongated fine-grained prisms; Figure 9a), consistent with theoretical calculations for SD grains with uniaxial anisotropy (Newell, 2005). In contrast, FORC diagrams for noninteracting grains with a small q (e.g., $q = 1.1$) show two symmetric low-coercivity peaks offset from the $B_u = 0$ axis and a central ridge peak (Figure 9b). The two symmetric peaks correspond to the nucleation and annihilation of single-vortex states (Roberts et al., 2014; Valdez-Grijalva et al., 2018) within the modeled nearly equidimensional particles. In the presence of interactions, the central ridge and the negative region show a vertical broadening, and an asymmetric teardrop is observed for $q = 1.5$

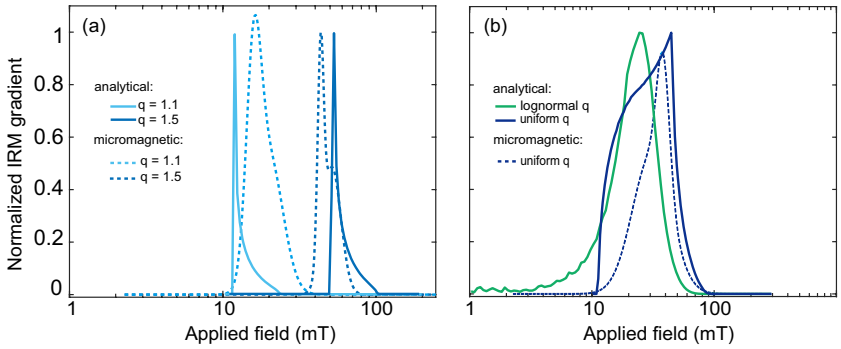

Figure 6. Analytical IRM derivative curves for noninteracting SD Stoner-Wohlfarth elongated grains with (a) $q = 1.1$, $q = 1.5$, and (b) a uniform q and lognormal distribution of q within 1 to 1–1.5. Solid lines: analytical simulated IRM curves. Dashed lines: micromagnetic simulated IRM curves for noninteracting elongated spheroids.

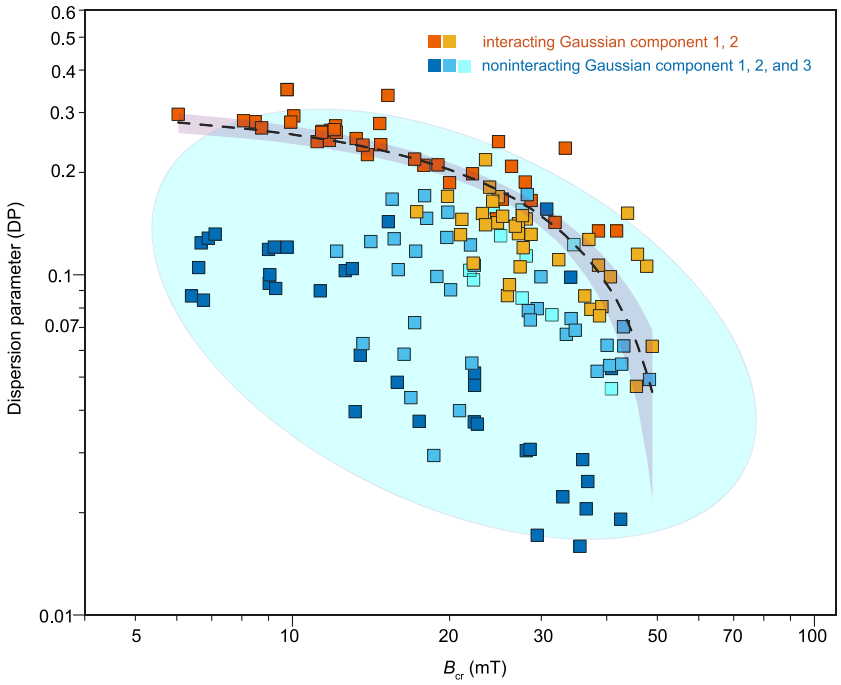

Figure 7. Summary of dispersion parameters (DP) against remanent coercivity (B_{cr}) for all micromagnetic simulated IRM derivative curves (i.e., q = 1.1, 1.2, 1.3, 1.4, 1.5, and 1–1.5 for elongated and flattened particles). Component 1, 2, and 3 represents Gaussian components with increasing B_{cr}. Dashed line indicates trend defined by a linear function with 95% confidence interval (gray area) for interacting Gaussian components. Blue area represents 95% confidence ellipse of IRM parameters for noninteracting Gaussian components.

(Figure 9c). For q = 1.1, the two symmetrical single-vortex peaks merge with the central ridge peak and a negative distribution occurs in the lower-right region (Figure 9d).

4. Discussion

4.1. Origin of Multiple Components in the Modeled IRM Curves

The sharp increase on the left and gradual decrease on the right of the IRM curves occurring for noninteracting elongated particles (Figures 2a–2f and S1–S3) is because B_{cr} is a function of the angle φ between the particle long axis and the applied field (Dunlop & Özdemir, 1997). Our micromagnetic and analytical calculations indicate relatively consistent B_{cr} values in the median φ range (e.g., for noninteracting elongated spheroids with q = 1.5; Figure 10) – this means that many particles at median angles reverse their magnetic moments almost simultaneously compared with those at other angles. Hence, the IRM curves show a sharp increase on the left and a gradual decrease on the right, which requires two Gaussian components to fit. The sharp increase is smoothed and broadened for q with a distribution (Figures 3a–3c) or in the presence of interactions (Figures 2g–2l). In addition, the sharp increase disappears for coarse-grained prismatic particles with q = 1.5 (Figure 5a), likely due to the co-existence of domain states (SD and vortex states). Different analytical IRM curves for particles with a uniform distribution q and a lognormal distribution of q (Figure 6b) is due to superimposition of noninteracting IRM components, which indicates the dominant effect of grain elongation distributions for noninteracting elongated fine-particle ensembles.

Switching types can also lead to multiple Gaussian components. Two switching types occur in the plane of long axes of noninteracting flattened prismatic and octahedral particles (e.g., for flattened prisms with q = 1.5): (a) switching along the long axes (Figure 11a) and (b) switching along the diagonal of the flattened plane (Figure 11b). B_{cr} are higher in case (1) than those in case (2). Such switching type produces IRM shoulders that require at least two Gaussian components to fit (e.g., Figures 2m–2r). It is expected that tri-

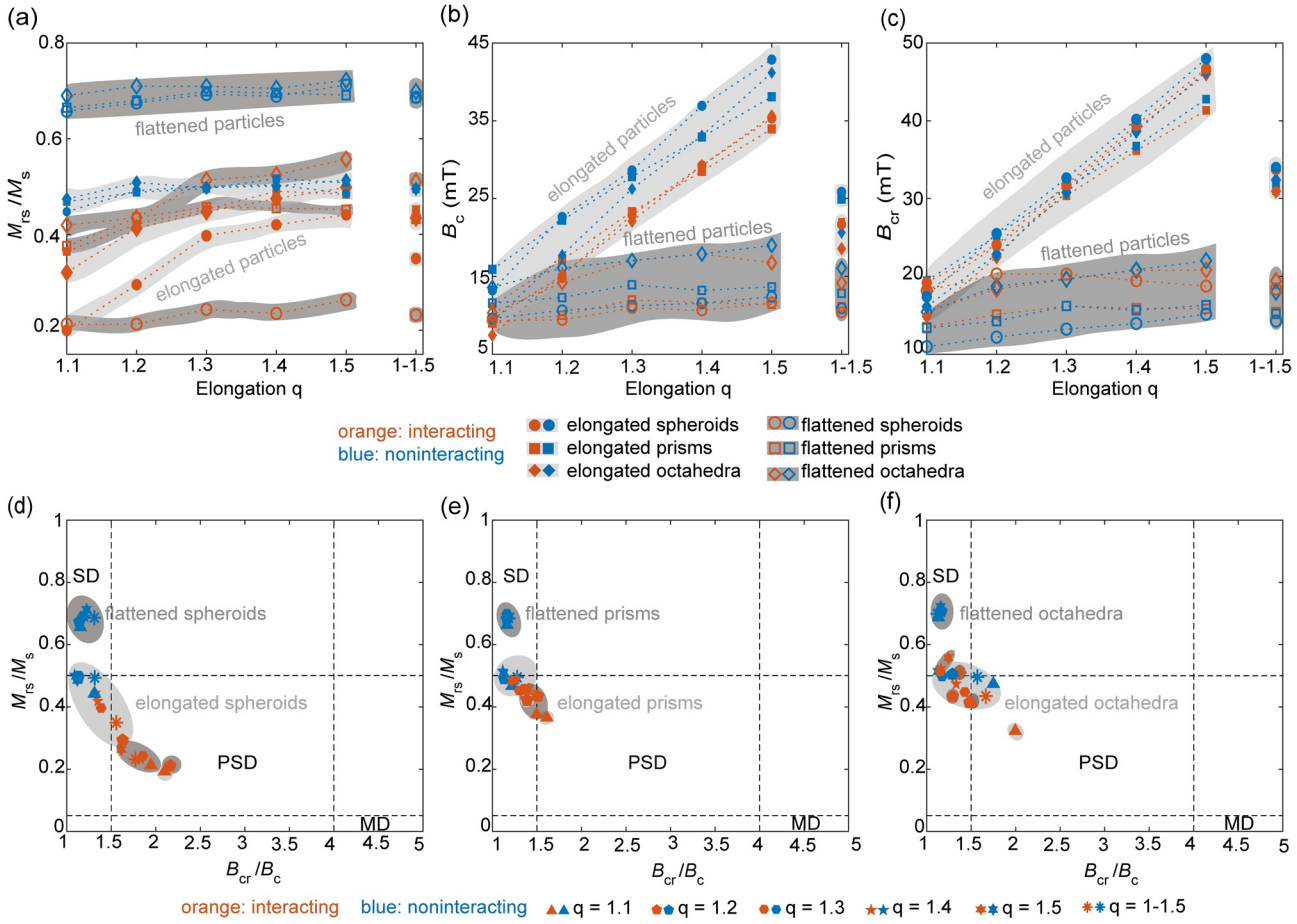

Figure 8. (a–c) Modeled hysteresis parameters (M_{rs}/M_s, B_c, and B_{cr}) versus elongation q. (d–f) Day plots (Day et al., 1977) for different modeled ensembles: both elongated and flattened fine-grained spheroids (d), prisms (e), and octahedra (f). In (d–f), data points in light and dark areas represent elongated and flattened grains, respectively. Orange and blue indicate interacting and noninteracting particles, respectively. SD: single domain; PSD: pseudo-single domain; MD: multidomain.

axiality anisotropy (i.e., three axes of the flattened particle are different in length) may also affect the IRM components for noninteracting particles. Interactions can suppress the shoulders and produce similar IRM curves (Figures 2s–2x and 3j–3l).

4.2. Effect of Magnetostatic Interactions on Hysteresis Parameters and FORC Diagrams

Our simulations indicate that hysteresis parameters (M_{rs}, B_c, and B_{cr}) for flattened interacting and noninteracting particles are almost independent of grain morphologies (Figures 8a–8f). Interactions, however, decrease M_{rs} and B_c and increase B_{cr}. In contrast, grain morphologies for elongated particles do affect hysteresis parameters, and interactions tend to decrease all of them (M_{rs}, B_c, and B_{cr}; Figures 8a–8c). B_c and B_{cr} values of flattened particles are lower than those of elongated grains. This is due to shape anisotropy: flattened particles have two long axes compared to elongated grains, which makes it easier to rotate the remanent magnetization in the flattened plane (Dunlop & Özdemir, 1997). Simulated hysteresis parameters show clear trends in the Day plot (Day et al., 1977, Figures 8d–8f): (a) all of them are concentrated in the top-left of the SD region for noninteracting flattened particles so that these particles can be easily detected, and (b) move toward PSD region due to interactions (e.g., Harrison et al., 2002; Muxworthy et al., 2003; Roberts et al., 2014; Sprowl, 1990) for both elongated and flattened grains. Noninteracting fine particles with small elongations (i.e., $q = 1.1$) can be distinguished from particles with large q in the FORC diagrams as distinct features: symmetric peaks offset from the central ridge and a central ridge peak (Figure 9b). Interactions can merge the symmetric peaks into a single broad peak in the FORC diagrams (Figure 9d).

Table 1
Simulated Hysteresis Parameters for the Noninteracting and Interacting Systems

		Noninteracting				Interacting			
Model	Elongation q	B_c (mT)	B_{cr} (mT)	M_{rs}/M_s	B_{cr}/B_c	B_c (mT)	B_{cr} (mT)	M_{rs}/M_s	B_{cr}/B_c
Elongated									
Spheroids	1.1	13.22	17.41	0.45	1.32	9.18	19.21	0.20	2.09
	1.2	22.62	25.48	0.49	1.13	14.82	24.10	0.30	1.63
	1.3	28.61	32.63	0.50	1.14	22.88	31.79	0.40	1.39
	1.4	36.93	40.17	0.50	1.09	29.24	39.44	0.42	1.35
	1.5	42.87	47.98	0.49	1.12	35.30	46.70	0.44	1.32
	1–1.5	25.85	33.98	0.49	1.31	21.66	33.74	0.35	1.56
Prisms	1.1	15.92	19.45	0.47	1.22	11.20	18.06	0.37	1.61
	1.2	22.20	25.24	0.49	1.14	17.15	23.93	0.42	1.40
	1.3	27.80	31.42	0.50	1.13	23.30	30.34	0.45	1.30
	1.4	32.91	36.73	0.52	1.12	28.48	36.15	0.49	1.27
	1.5	38.09	42.79	0.51	1.12	33.94	41.34	0.48	1.22
	1–1.5	24.92	31.86	0.49	1.28	22.00	30.98	0.45	1.41
Octahedra	1.1	9.17	16.13	0.47	1.76	7.45	14.89	0.32	2.00
	1.2	17.75	22.86	0.51	1.29	15.24	22.51	0.41	1.48
	1.3	26.23	30.79	0.50	1.17	22.08	31.45	0.45	1.42
	1.4	33.08	38.64	0.50	1.17	29.23	38.93	0.47	1.33
	1.5	41.18	46.34	0.51	1.13	35.62	46.01	0.50	1.29
	1–1.5	20.61	32.37	0.50	1.57	18.58	30.94	0.43	1.67
Flattened									
Spheroids	1.1	9.61	10.97	0.66	1.14	9.32	18.18	0.21	1.95
	1.2	10.64	12.20	0.67	1.15	9.41	20.32	0.21	2.16
	1.3	11.22	13.23	0.69	1.18	10.94	20.30	0.24	1.86
	1.4	11.56	13.95	0.69	1.21	10.65	19.48	0.24	1.83
	1.5	12.40	15.17	0.71	1.22	11.63	18.76	0.26	1.61
	1–1.5	10.90	14.28	0.69	1.31	10.39	18.40	0.23	1.77
Prisms	1.1	11.58	13.37	0.66	1.15	9.01	13.48	0.38	1.50
	1.2	12.30	14.26	0.68	1.16	10.02	15.11	0.43	1.51
	1.3	13.94	16.22	0.70	1.16	11.98	16.20	0.46	1.35
	1.4	13.21	15.66	0.70	1.19	11.66	15.92	0.45	1.36
	1.5	13.67	16.32	0.69	1.19	11.41	15.84	0.45	1.39
	1–1.5	12.85	15.19	0.69	1.18	11.11	15.44	0.43	1.39
Octahedra	1.1	13.58	15.44	0.69	1.14	10.31	15.44	0.42	1.50
	1.2	16.10	18.75	0.71	1.16	14.22	18.37	0.43	1.29
	1.3	17.05	19.69	0.71	1.15	17.05	19.63	0.51	1.15
	1.4	17.89	20.86	0.71	1.17	17.89	20.78	0.52	1.16
	1.5	19.02	22.03	0.72	1.16	16.77	20.84	0.56	1.24
	1–1.5	16.07	17.99	0.70	1.12	14.17	19.45	0.51	1.37

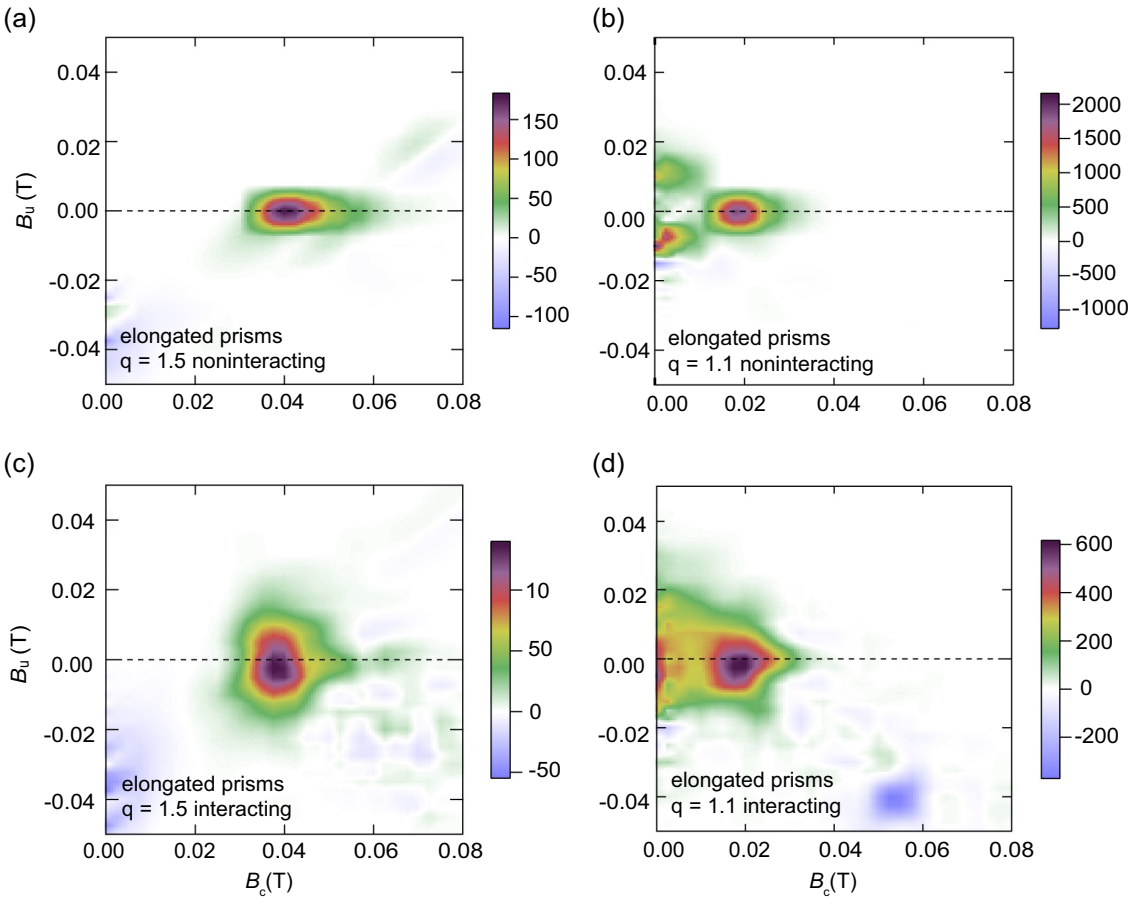

Figure 9. Modeled FORC diagrams (SF = 4) for (a), (b) noninteracting and (c), (d) interacting elongated fine-grained prisms with $q = 1.5$ and $q = 1.1$, respectively.

4.3. Implications for Magnetic Mineral Identification

The simulation results presented here have important implications for identifying natural magnetic minerals, since IRM curves even for well-controlled synthetic magnetite (Dunlop, 1973) and magnetite magnetosome samples (Jovane et al., 2012; Li et al., 2012) can produce multiple Gaussian components (Figure S7). Our modeled magnetic particle ensembles resemble some magnetic mineral populations and microstructures observed within natural samples, such as fine-grained magnetic mineral inclusions in silicates (e.g., Chang et al., 2016; Zhou et al., 1999) and close-packed diagenetic greigite grain clusters in iron sulfide intergrowth (Roberts et al., 2011). It is noted that our IRM Gaussian component analysis results and the relationship between DP and B_{cr} (Figures 2, 3, and 7) for interacting grains are similar to results of samples containing bacterial magnetic minerals with a detrital and extracellular (D + EX) and a biogenic soft or hard (BS/BH) coercivity distribution (e.g., Abrajevitch & Kodama, 2009; Chang et al., 2013; Egli, 2004a, 2004b; Vasiliev et al., 2007, 2008; Yamazaki, 2008, 2009). Hence, care should be taken when interpreting the IRM signature for magnetosome identifications (Berndt et al., 2020; Chang et al., 2019). Therefore, additional rock magnetic measurements, such as FORC diagrams, are necessary to identify the presence of interactions. For example, the simulated FORC diagrams for interacting grains contain apparent broad vertical distributions (Figure 9c), which are distinct from the narrow central-ridge signature for magnetosome-bearing samples (e.g., Egli et al., 2010; Roberts et al., 2012).

Our simulations indicate that IRM curves commonly require multiple Gaussian components to be fitted even for magnetic mineral assemblages with a simple grain size distribution (e.g., Egli, 2003, 2004a, 2004b; Heslop et al., 2004; Robertson & France, 1994). We found that three main factors can produce multiple IRM Gaussian components: (a) the distribution of grain elongations, for example, a uniform q and a lognor-

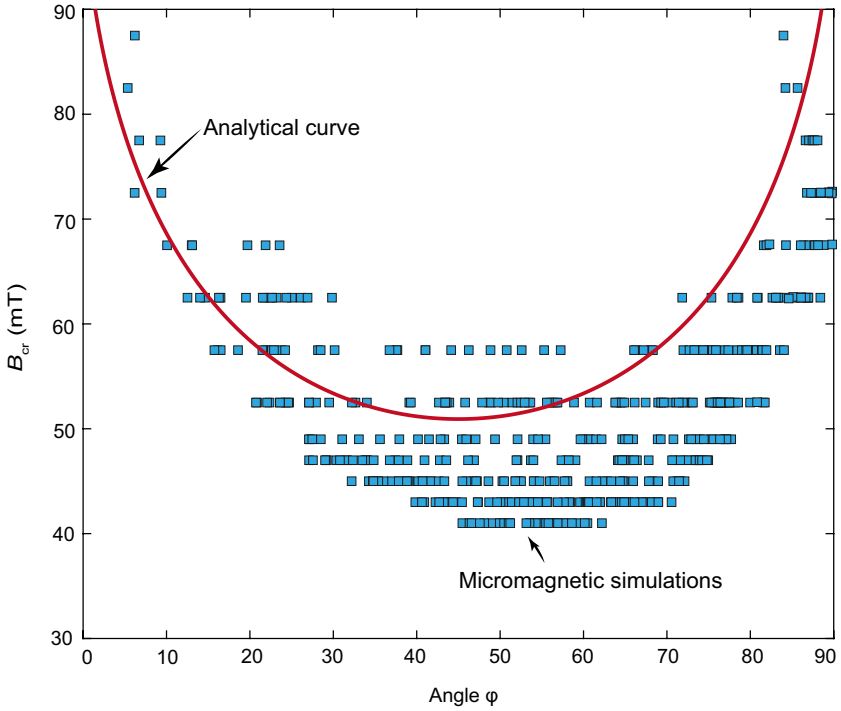

Figure 10. B_{cr} variations as a function of the angle φ between the particle long axis and the applied field for noninteracting elongated spheroids with $q = 1.5$. Blue squares and red solid line are micromagnetic and analytical simulation results, respectively. Micromagnetic simulations (blue squares) are drawn through 10 spheroid clusters.

mal distribution of q can cause two Gaussian components, (b) switching types for noninteracting flattened prismatic and octahedral particles can lead to two coercivity distributions, and (c) magnetostatic interactions cause two overlapping Gaussian components. While our simulations provide important constraints for understanding the IRM curves of natural samples, intrinsic uncertainties and limitations remain with our micromagnetic models that have restricted modeling parameter space. For instance, the easy axis in natural magnetite samples is not necessarily along the [1 1 1] axis especially for irregularly shaped quasi-equidimensional realistic particles. Furthermore, SD magnetite particles can be partially oxidized resulting in a distribution of cubic anisotropy constants. Variable shapes of SD assemblages in the abiogenic case should also be considered. So the simulation results here should be considered only as possible outcomes of natural components. Some multiple Gaussian components in our simulations can also be modeled with one skewed generalized Gaussian (SGG) distribution proposed by Egli (2003, 2004a). For example, IRM curves for noninteracting elongated particles (Figures 2a–2f) can be fitted with only one right-skewness SGG component. Hence, it appears that SGG functions are more suitable for IRM curves of noninteracting elongated particles than CLG functions. In contrast, IRM curves for noninteracting flattened particles (Figures 2m–2r) fitted using CLG functions is simpler than SGG functions. Therefore, fitting method should be selected carefully (He et al., 2020). Also, other direct methods for magnetic mineral identification, for example, electron microscopic observations, are highly useful to constrain results from IRM measurements (e.g., identifying grain morphologies and microstructures).

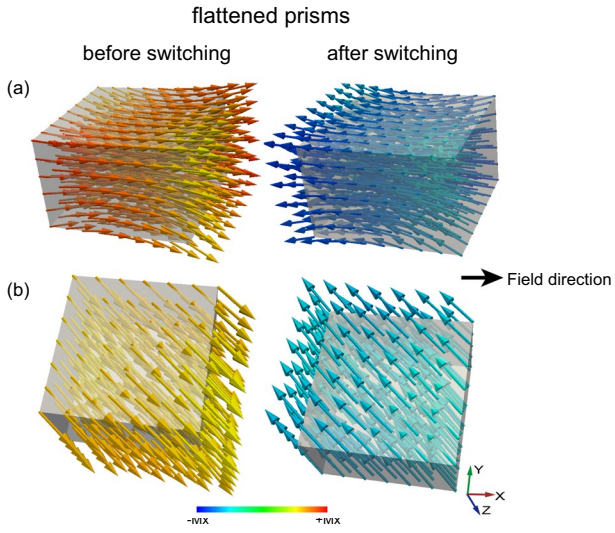

Figure 11. Remanent domain states before and after switching that show two switching types (a) switching along the long axes of the plane, and (b) switching along the diagonal of the plane for noninteracting flattened prisms with $q = 1.5$. Magnetizations are colored according to the degree of alignment with the x-axis. Red and blue illustrate magnetizations are strong and weak along the x-axis, respectively.

5. Conclusions

The following conclusions can be made about IRM curves from our micromagnetic calculations: (a) magnetostatic interactions generally decrease hysteresis parameters (M_{rs}, B_c, and B_{cr}) – with the only exception of generally increasing B_{cr} for flattened grains, (b) the shape of IRM curves for noninteracting fine-grained particles are almost determined by the elongation distribution of particle and the particle shape (i.e., elongated and flattened particles), (c) IRM derivative curves for interacting flattened particles have similar asymmetric features regardless of grain morphology, and (d) multiple Gaussian components do not necessarily reflect multiple magnetic mineral populations both for interacting and noninteracting particles. For example, a simple grain size distribution of interacting elongated grain assemblages can have IRM curves similar to some magnetosome-bearing samples with a D + EX and a BS/BH coercivity distribution.

Data Availability Statement

Simulated datasets in this study are available in the supplementary information Tables S1 and S2. Data of mesh files and simulated magnetization curves are available at the Peking University Open Research Data Platform (https://doi.org/10.18170/DVN/Y7PNMR).

Acknowledgments
This study was supported by the National Natural Science Foundation of China (NSFC grants 41974074, 42061130214, 41722402). L. Chang acknowledges additional support from a Royal Society-Newton Advanced Fellowship (NAF\R1\201096). We thank Wyn Williams for insightful discussions, Mark Dekkers for efficient editorial handling, and two anonymous reviewers and an associate editor for providing constructive comments that improved this paper.

References

Abrajevitch, A., & Kodama, K. (2009). Biochemical vs. detrital mechanism of remanence acquisition in marine carbonates: A lesson from the K–T boundary interval. *Earth and Planetary Science Letters*, *286*(1), 269–277. https://doi.org/10.1016/j.epsl.2009.06.035

Ahrens, J., Geveci, B., & Law, C. (2005). ParaView: An end-user tool for large-data visualization. In C. D. Hansen, & C. R. Johnson (Eds.), *The visualization handbook* (pp. 717–731). Elsevier. https://doi.org/10.1016/B978-012387582-2/50038-1

Ayachit, U. (2015). *The ParaView guide: A parallel visualization application*. Kitware.

Berndt, T. A., Chang, L., & Pei, Z. (2020). Mind the gap: Towards a biogenic magnetite palaeoenvironmental proxy through an extensive finite-element micromagnetic simulation. *Earth and Planetary Science Letters*, *532*, 116010. https://doi.org/10.1016/j.epsl.2019.116010

Chang, L., Harrison, R. J., & Berndt, T. A. (2019). Micromagnetic simulation of magnetofossils with realistic size and shape distributions: Linking magnetic proxies with nanoscale observations and implications for magnetofossil identification. *Earth and Planetary Science Letters*, *527*, 115790. https://doi.org/10.1016/j.epsl.2019.115790

Chang, L., Roberts, A. P., Heslop, D., Hayashida, A., Li, J., Zhao, X., et al. (2016). Widespread occurrence of silicate-hosted magnetic mineral inclusions in marine sediments and their contribution to paleomagnetic recording. *Journal of Geophysical Research: Solid Earth*, *121*(12), 8415–8431. https://doi.org/10.1002/2016JB013109

Chang, L., Winklhofer, M., Roberts, A. P., Heslop, D., Florindo, F., Dekkers, M. J., et al. (2013). Low-temperature magnetic properties of pelagic carbonates: Oxidation of biogenic magnetite and identification of magnetosome chains. *Journal of Geophysical Research: Solid Earth*, *118*(12), 6049–6065. https://doi.org/10.1002/2013JB010381

Day, R., Fuller, M., & Schmidt, V. A. (1977). Hysteresis properties of titanomagnetites: Grain-size and compositional dependence. *Physics of the Earth and Planetary Interiors*, *13*(4), 260–267. https://doi.org/10.1016/0031-9201(77)90108-X

Dunlop, D. J. (1973). Thermoremanent magnetization in submicroscopic magnetite. *Journal of Geophysical Research*, *78*(32), 7602–7613. https://doi.org/10.1029/JB078i032p07602

Dunlop, D. J., & Özdemir, Ö. (1997). *Rock magnetism: Fundamentals and frontiers* (p. 573). Cambridge University Press. https://doi.org/10.1017/CBO9780511612794

Egli, R. (2003). Analysis of the field dependence of remanent magnetization curves. *Journal of Geophysical Research: Solid Earth*, *108*(B2), 2081. https://doi.org/10.1029/2002JB002023

Egli, R. (2004a). Characterization of individual rock magnetic components by analysis of remanence curves, 1. unmixing natural sediments. *Studia Geophysica et Geodaetica*, *48*(2), 391–446. https://doi.org/10.1023/B:SGEG.0000020839.45304.6d

Egli, R. (2004b). Characterization of individual rock magnetic components by analysis of remanence curves. 2. fundamental properties of coercivity distributions. *Physics and Chemistry of the Earth*, *29*(13–14), 851–867. https://doi.org/10.1016/j.pce.2004.04.001

Egli, R., Chen, A. P., Winklhofer, M., Kodama, K. P., & Horng, C.-S. (2010). Detection of noninteracting single domain particles using first-order reversal curve diagrams. *Geochemistry, Geophysics, Geosystems*, *11*, Q01Z11. https://doi.org/10.1029/2009GC002916

Fabian, K., & von Dobeneck, T. (1997). Isothermal magnetization of samples with stable Preisach function: A survey of hysteresis, remanence, and rock magnetic parameters. *Journal of Geophysical Research: Solid Earth*, *102*(B8), 17659–17677. https://doi.org/10.1029/97JB01051

Fearon, M., Chantrell, R. W., & Wohlfarth, E. P. (1990). A theoretical study of interaction effects on the remanence curves of particulate dispersions. *Journal of Magnetism and Magnetic Materials*, *86*(2–3), 197–206. https://doi.org/10.1016/0304-8853(90)90121-6

Ge, K., & Liu, Q. (2014). Effects of the grain size distribution on magnetic properties of magnetite: Constraints from micromagnetic modeling. *Chinese Science Bulletin*, *59*(34), 4763–4773. https://doi.org/10.1007/s11434-014-0584-z

Harrison, R. J., Dunin-Borkowski, R. E., & Putnis, A. (2002). Direct imaging of nanoscale magnetic interactions in minerals. *Proceedings of the National Academy of Sciences of the United States of America*, *99*(26), 16556–16561. https://doi.org/10.1073/pnas.262514499

Harrison, R. J., & Feinberg, J. M. (2008). FORCinel: An improved algorithm for calculating first-order reversal curve distributions using locally weighted regression smoothing. *Geochemistry, Geophysics, Geosystems*, *9*(5), Q05016. https://doi.org/10.1029/2008GC001987

Harrison, R. J., & Lascu, I. (2014). FORCulator: A micromagnetic tool for simulating first-order reversal curve diagrams. *Geochemistry, Geophysics, Geosystems*, *15*(12), 4671–4691. https://doi.org/10.1002/2014GC005582

He, K., Zhao, X., Pan, Y., Zhao, X., Qin, H., & Zhang, T. (2020). Benchmarking component analysis of remanent magnetization curves with a synthetic mixture series: Insight into the reliability of unmixing natural samples. *Journal of Geophysical Research. Solid Earth*, *125*(10), e2020JB020105. https://doi.org/10.1029/2020JB020105

Heslop, D. (2015). Numerical strategies for magnetic mineral unmixing. *Earth-Science Reviews*, *150*, 256–284. https://doi.org/10.1016/j.earscirev.2015.07.007

Heslop, D., Dekkers, M. J., Kruiver, P. P., & van Oorschot, I. H. M. (2002). Analysis of isothermal remanent magnetization acquisition curves using the expectation-maximization algorithm. *Geophysical Journal International*, *148*(1), 58–64. https://doi.org/10.1046/j.0956-540x.2001.01558.x

Heslop, D., & Dillon, M. (2007). Unmixing magnetic remanence curves without a priori knowledge. *Geophysical Journal International*, *170*(2), 556–566. https://doi.org/10.1111/j.1365-246X.2007.03432.x

Heslop, D., McIntosh, G., & Dekkers, M. J. (2004). Using time- and temperature-dependent Preisach models to investigate the limitations of modelling isothermal remanent magnetization acquisition curves with cumulative log Gaussian functions. *Geophysical Journal International*, *157*(1), 55–63. https://doi.org/10.1111/j.1365-246X.2004.02155.x

Jovane, L., Florindo, F., Bazylinski, D. A., & Lins, U. (2012). Prismatic magnetite magnetosomes from cultivated Magnetovibrio blakemorei strain MV-1: A magnetic fingerprint in marine sediments? *Environmental Microbiology Reports*, *4*(6), 664–668. https://doi.org/10.1111/1758-2229.12000

Kruiver, P. P., Dekkers, M. J., & Heslop, D. (2001). Quantification of magnetic coercivity components by the analysis of acquisition curves of isothermal remanent magnetisation. *Earth and Planetary Science Letters*, *189*(3–4), 269–276. https://doi.org/10.1016/S0012-821X(01)00367-3

Lees, J. A. (1997). Mineral magnetic properties of mixtures of environmental and synthetic materials: Linear additivity and interaction effects. *Geophysical Journal International*, *131*(2), 335–346. https://doi.org/10.1111/j.1365-246X.1997.tb01226.x

Li, J., Wu, W., Liu, Q., & Pan, Y. (2012). Magnetic anisotropy, magnetostatic interactions and identification of magnetofossils. *Geochemistry, Geophysics, Geosystems*, *13*(12), Q10Z51. https://doi.org/10.1029/2012GC004384

Maxbauer, D. P., Feinberg, J. M., & Fox, D. L. (2016). MAX UnMix: A web application for unmixing magnetic coercivity distributions. *Computers & Geosciences*, *95*, 140–145. https://doi.org/10.1016/j.cageo.2016.07.009

Maxbauer, D. P., Feinberg, J. M., Fox, D. L., & Nater, E. A. (2017). Response of pedogenic magnetite to changing vegetation in soils developed under uniform climate, topography, and parent material. *Scientific Reports*, *7*(1), 17575. https://doi.org/10.1038/s41598-017-17722-2

Muxworthy, A., Williams, W., & Virdee, D. (2003). Effect of magnetostatic interactions on the hysteresis parameters of single-domain and pseudo-single-domain grains. *Journal of Geophysical Research – Solid Earth*, *108*(B11), 2517. https://doi.org/10.1029/2003JB002588

Newell, A. J. (2005). A high-precision model of first-order reversal curve (FORC) functions for single-domain ferromagnets with uniaxial anisotropy. *Geochemistry, Geophysics, Geosystems*, *6*(5), Q05010. https://doi.org/10.1029/2004GC000877

Nikolaisen, E. S., Harrison, R. J., Fabian, K., & McEnroe, S. A. (2020). Hysteresis of natural magnetite ensembles: Micromagnetics of silicate-hosted magnetite inclusions based on focused-ion-beam nanotomography. *Geochemistry, Geophysics, Geosystems*, *21*, e2020GC009389. https://doi.org/10.1029/2020GC009389

Ó Conbhuí, P., Williams, W., Fabian, K., Ridley, P., Nagy, L., & Muxworthy, A. R. (2018). MERRILL: Micromagnetic earth related robust interpreted language laboratory. *Geochemistry, Geophysics, Geosystems*, *19*(4), 1080–1106. https://doi.org/10.1002/2017GC007279

Osborn, J. A. (1945). Demagnetizing factors of the general ellipsoid. *Physical Review*, *67*(11–12), 351–357. https://doi.org/10.1103/PhysRev.67.351

Roberts, A. P., Chang, L., Heslop, D., Florindo, F., & Larrasoaña, J. C. (2012). Searching for single domain magnetite in the pseudo-single domain sedimentary haystack: Implications of biogenic magnetite preservation for sediment magnetism and relative paleointensity determinations. *Journal of Geophysical Research*, *117*, B08104. https://doi.org/10.1029/2012JB009412

Roberts, A. P., Chang, L., Rowan, C. J., Horng, C., & Florindo, F. (2011). Magnetic properties of sedimentary greigite (Fe_3S_4): An update. *Reviews of Geophysics*, *49*(1), RG1002. https://doi.org/10.1029/2010rg000336

Roberts, A. P., Heslop, D., Zhao, X., & Pike, C. R. (2014). Understanding fine magnetic particle systems through use of first-order reversal curve diagrams. *Reviews of Geophysics*, *52*(4), 557–602. https://doi.org/10.1002/2014RG000462

Roberts, A. P., Hu, P., Harrison, R. J., Heslop, D., Muxworthy, A. R., Oda, H., et al. (2019). Domain state diagnosis in rock magnetism: Evaluation of potential alternatives to the day diagram. *Journal of Geophysical Research: Solid Earth*, *124*(6), 5286–5314. https://doi.org/10.1029/2018JB017049

Roberts, A. P., Pike, C. R., & Verosub, K. L. (2000). First-order reversal curve diagrams: A new tool for characterizing the magnetic properties of natural samples. *Journal of Geophysical Research: Solid Earth*, *105*(B12), 28461–28475. https://doi.org/10.1029/2000JB900326

Robertson, D. J., & France, D. E. (1994). Discrimination of remanence-carrying minerals in mixtures, using isothermal remanent magnetisation acquisition curves. *Physics of the Earth and Planetary Interiors*, *82*(3–4), 223–234. https://doi.org/10.1016/0031-9201(94)90074-4

Sprowl, D. R. (1990). Numerical estimation of interactive effects in single-domain magnetite. *Geophysical Research Letters*, *17*(11), 2009–2012. https://doi.org/10.1029/GL017i011p02009

Stockhausen, H. (1998). Some new aspects for the modelling of isothermal remanent magnetization acquisition curves by cumulative log Gaussian functions. *Geophysical Research Letters*, *25*(12), 2217–2220. https://doi.org/10.1029/98GL01580

Stoner, E. C., & Wohlfarth, E. P. (1948). A mechanism of magnetic hysteresis in heterogeneous alloys. *IEEE Transactions on Magnetics*, *27*(4), 3475–3518. https://doi.org/10.1109/TMAG.1991.1183750

Trelis (2021). *(Version 2021.3) [computer software]*. Coreform LLC. Retrieved from http://coreform.com

Valdez-Grijalva, M. A., Muxworthy, A. R., Williams, W., Ó Conbhuí, P., Nagy, L., Roberts, A. P., & Heslop, D. (2018). Magnetic vortex effects on first-order reversal curve (FORC) diagrams for greigite dispersions. *Earth and Planetary Science Letters*, *501*, 103–111. https://doi.org/10.1016/j.epsl.2018.08.027

Vasiliev, I., Dekkers, M. J., Krijgsman, W., Franke, C., Langereis, C. G., & Mullender, T. A. T. (2007). Early diagenetic greigite as a recorder of the paleomagnetic signal in Miocene-Pliocene sedimentary rocks of the Carpathian foredeep (Romania). *Geophysical Journal International*, *171*(2), 613–629. https://doi.org/10.1111/j.1365-246X.2007.03560.x

Vasiliev, I., Franke, C., Meeldijk, J. D., Dekkers, M. J., Langereis, C. G., & Krijgsman, W. (2008). Putative greigite magnetofossils from the Pliocene epoch. *Nature Geoscience*, *1*(11), 782–786. https://doi.org/10.1038/ngeo335

Yamazaki, T. (2008). Magnetostatic interactions in deep-sea sediments inferred from first-order reversal curve diagrams: Implications for relative paleointensity normalization. *Geochemistry, Geophysics, Geosystems*, *9*(2), Q02005. https://doi.org/10.1029/2007GC001797

Yamazaki, T. (2009). Environmental magnetism of Pleistocene sediments in the north pacific and Ontong-Java Plateau: Temporal variations of detrital and biogenic components. *Geochemistry, Geophysics, Geosystems*, *10*(7), Q07Z04. https://doi.org/10.1029/2009GC002413

Zhou, W., Van der Voo, R., & Peacor, D. R. (1999). Preservation of pristine titanomagnetite in older ocean-floor basalts and its significance for paleo-intensity studies. *Geology*, *27*, 1043–1046. https://doi.org/10.1130/0091-7613(1999)027<1043:POPTIO>2.3.CO;2